Constraints on high density equation of state from maximum neutron star mass

Márcio Ferreira[*] and Constança Providência[†]

CFisUC, Department of Physics, University of Coimbra, P-3004—516 Coimbra, Portugal

(Received 25 June 2021; accepted 1 August 2021; published 2 September 2021)

The low density nuclear matter equation of state is strongly constrained by nuclear properties; however, for constraining the high density equation of state it is necessary to resort to indirect information obtained from the observation of neutron stars, compact objects that may have a central density several times nuclear matter saturation density, n_0. Taking a metamodeling approach to generate a huge set of equations of state that satisfy nuclear matter properties close to n_0 and that do not contain a first-order phase transition, the possibility of constraining the high density equation of state (EOS) was investigated. The entire information obtained from the GW170817 event for the probability distribution of $\tilde{\Lambda}$ was used to make a probabilistic inference of the EOS, which goes beyond the constraints imposed by nuclear matter properties. Nuclear matter properties close to saturation, below $2n_0$, do not allow us to distinguish between equations of state that predict different neutron star (NS) maximum masses. This is, however, not true if the equation of state is constrained at low densities by the tidal deformability of the NS merger associated to GW170817. Above $3n_0$, differences may be large, for both approaches, and, in particular, the pressure and speed of sound of the sets studied do not overlap, showing that the knowledge of the NS maximum mass may give important information on the high density EOS. Narrowing the maximum mass uncertainty interval will have a sizable effect on constraining the high density EOS.

DOI: 10.1103/PhysRevD.104.063006

I. INTRODUCTION

Neutron stars (NSs) are special astrophysical objects through which the properties of cold superdense neutron-rich nuclear matter may be investigated. The massive NSs observed, e.g., PSR J1614 − 2230 with $M = 1.908 \pm 0.016\ M_\odot$ [1–3], have established strong constraints on the equation of state (EOS) of nuclear matter. Further pulsar observations, PSR J0348 + 0432 with $M = 2.01 \pm 0.04\ M_\odot$ [4] and MSP J0740 + 6620, with mass $2.08^{+0.07}_{-0.07}\ M_\odot$ [5,6] and radius $12.39^{+1.30}_{-0.98}$ km obtained from NICER and XMM-Newton data [7] (together with an updated mass $2.072^{+0.067}_{-0.066}\ M_\odot$), have strengthened the already stiff constraints on the EOS. The NICER mission [8] has estimated the mass and radius of the pulsar PSR J0030 − 0451: respectively, $1.34^{+0.15}_{-0.16}\ M_\odot$, $12.71^{+1.14}_{-1.19}$ km [9] and $1.44^{+0.15}_{-0.15}\ M_\odot$, $13.02^{+1.24}_{-1.06}$ km [10].

Gravitational waves (GWs) are another crucial source of information about NS matter. GWs are emitted during the coalescence of binary NS systems and carry important information on the high density properties of the EOS. The analysis of the event GW170817 has settled an upper bound on the effective tidal deformability of the binary $\tilde{\Lambda}$ [11]. Using a low-spin prior, which is consistent with the observed NS population, the value $\tilde{\Lambda} \leq 800$ (90% confidence) was determined from the GW170817 event. Tighter constraints were found in a follow-up reanalysis [12], with $\tilde{\Lambda} = 300^{+420}_{-230}$ (90% confidence), under minimal assumptions about the nature of the compact objects. The two NS radii for the GW170817 event were estimated in [13], under the hypothesis that both NSs are described by the same EOS and have spins within the range observed in Galactic binary NSs, to be $R_1 = 11.9^{+1.4}_{-1.4}$ km (heavier star) and $R_2 = 11.9^{+1.4}_{-1.4}$ km (lighter star). These constraints on $R_{1,2}$ were obtained requiring that the EOS supports NSs with masses larger than $1.97\ M_\odot$.

The detection of GWs from the GW170817 event was followed by electromagnetic counterparts, the gamma-ray burst (GRB) GRB170817A [14] and the electromagnetic transient AT2017gfo [15], that set extra constraints on the lower limit of the tidal deformability [16–20]. This last constraint seems to rule out very soft EOS: the lower limit of the tidal deformability of a $1.37\ M_\odot$ star set by the above studies limits the tidal deformability to $\Lambda_{1.37\ M_\odot} > 210$ [18], 300 [17], 279 [19], and 309 [20].

The LIGO/Virgo Collaboration has recently reported the gravitational-wave observation of a compact binary

[*]marcio.ferreira@uc.pt
[†]cp@uc.pt

coalescence (GW190814) [21]. While the primary component of GW190814 is conclusively a black hole of mass 22.2–24.3 $M_\odot$, the secondary component of the binary with mass 2.50–2.67 $M_\odot$ remains yet inconclusive, which might be either the heaviest neutron star or the lightest black hole ever discovered in a double compact-object system [21]. The absence of measurable tidal deformations and the absence of an electromagnetic counterpart from the GW190814 event are consistent in both scenarios [21]. The uncertainty on the nature of the second component has prompted an ongoing debate on whether the EOS of nuclear matter is able to accommodate such a massive NS.

In the present study, we will analyze which information on the high density EOS can be drawn from the knowledge of the NS maximum mass. Several works have estimated NS maximum mass using different approaches taking into account the GW170817 observation, the electromagnetic follow-up or/and NICER PSR J0030 + 0451 data [22–27]: the upper limit was fixed at ≈2.15–2.25 $M_\odot$ in [22] and updated to $M_{\rm max} < 2.3\ M_\odot$ in [26]; the interval $2.01^{+0.04}_{-0.04} \leq M_{\rm max}/M_\odot \leq 2.26^{+0.17}_{-0.15}$ was obtained for a nonrotating NS in [25]; [23] places the upper limit $M_{\rm max} \lesssim 2.17\ M_\odot$ (90%); in [24] the limits $2.0 < M_{\rm max}/M_\odot < 2.2$ (68%) and $2.0 < M_{\rm max}/M_\odot < 2.6 M_\odot$ (90%) have been obtained; in [28] the maximum mass 2.16–2.28 $M_\odot$ was calculated; in a recent study considering hybrid stars and both the GW170817 and the NICER observations the limits $2.36^{+0.49}_{-0.26}\ M_\odot$ and $2.39^{+0.47}_{-0.28}\ M_\odot$, taking two different hadronic models, were obtained at 90% credible interval [27]. Considering that a black hole was formed in GW170817 and taking conservative assumptions the authors of [29] concluded that the maximum mass should be $< 2.53\ M_\odot$.

We assume that no first-order phase transition occurs. Although restrictive, this hypothesis is supported by recent studies. In [30], a one-branch EOS was favored considering a nonparametric EOS model based on Gaussian processes and taking as constraints radio, x-ray and GW NS data, including the mass and radius measurement of the pulsar J0740 + 6620. A similar result was obtained in [31] t, where a first-order phase transition inside NSs was shown to be not favored, although not ruled out.

Nuclear matter properties are reasonably well constrained for densities below twice the saturation density by nuclear experiments. Therefore, as a second assumption, we take this information into account by considering a set of meta-EOSs that satisfy experimental nuclear matter constraints below $\approx 2n_0$ and give rise to thermodynamically consistent EOSs that describe 1.97 $M_\odot$ NSs. Applying a probabilistic approach, we analyze how the information contained in the entire posterior probability distribution (PDF) for the binary tidal deformability of the GW170817 event [32] affects the EOS pressure and speed of sound at high densities. It will be shown that nonoverlapping 90% credible intervals are obtained when different maximum masses are considered, indicating that a maximum mass constraint gives information on the star EOS. However, we should keep in mind that there is always the possibility that the "real" nuclear matter EOS consists in an unlikely realization for any probabilistic analysis approach, and thus the real EOS might actually be realized in a low-probability region. It is the nuclear force that determines the characteristics of the EOS. Having this in mind in most of our plots we represent the extremes of our sets.

The paper is organized as follows. The EOS parametrization and the method for generating the EOSs are presented in Sec. II. The results are discussed in Sec. III, where we analyze the properties of the different EOS datasets and perform a probabilistic inference on the high density region of the EOS. Finally, the conclusions are drawn in Sec. IV.

II. EOS MODELING

We assume the generic functional form for the energy per particle of homogeneous nuclear matter:

$$\mathcal{E}(n,\delta) = e_{\rm sat}(n) + e_{\rm sym}(n)\delta^2 \tag{1}$$

with

$$e_{\rm sat}(n) = E_{\rm sat} + \frac{1}{2}K_{\rm sat}x^2 + \frac{1}{6}Q_{\rm sat}x^3 + \frac{1}{24}Z_{\rm sat}x^4, \tag{2}$$

$$e_{\rm sym}(n) = E_{\rm sym} + L_{\rm sym}x + \frac{1}{2}K_{\rm sym}x^2 + \frac{1}{6}Q_{\rm sym}x^3 + \frac{1}{24}Z_{\rm sym}x^4, \tag{3}$$

where $x = (n - n_0)/(3n_0)$. The baryon density is given by $n = n_n + n_p$ and $\delta = (n_n - n_p)/n$ is the asymmetry, with n_n and n_p denoting the neutron and proton densities, respectively. This approach of Taylor expanding the energy functional up to fourth order around the saturation density, n_0, has been applied recently in several works [33–36]. The empirical parameters can be identified as the coefficients of the expansion. The isoscalar empirical parameters are defined as successive density derivatives of $e_{\rm sat}$, $P^k_{\rm is} = (3n_0)^k \partial^k e_{\rm sat}/\partial n^k$ for symmetrical nuclear matter at saturation, i.e., at $(\delta = 0, n = n_0)$, while the isovector parameters are connected to the density derivatives of $e_{\rm sym}$, $P^k_{\rm iv} = (3n_0)^k \partial^k e_{\rm sym}/\partial n^k$ also at $(\delta = 0, n = n_0)$.

Each EOS, denoted by index i, is represented by a point in the eight-dimensional space of parameters

$$\mathrm{EOS}_i = (E_{\rm sym}, L_{\rm sym}, K_{\rm sat}, K_{\rm sym}, Q_{\rm sat}, Q_{\rm sym}, Z_{\rm sat}, Z_{\rm sym})_i. \tag{4}$$

A set of EOSs is generated by drawing random samples through a multivariate Gaussian distribution:

TABLE I. The means $\bar{P}_i$ and standard deviations σ_{P_i} that characterize the multivariate Gaussian distribution [Eq. (5)]. All the quantities are in units of MeV.

P_i	$E_{\rm sym}$	$L_{\rm sym}$	$K_{\rm sat}$	$K_{\rm sym}$	$Q_{\rm sat}$	$Q_{\rm sym}$	$Z_{\rm sat}$	$Z_{\rm sym}$
$\bar{P}_i$	32	60	230	−100	300	0	−500	−500
σ_{P_i}	2	15	20	100	400	400	1000	1000

$$\mathrm{EOS}_i \sim N(\boldsymbol{\mu}, \boldsymbol{\Sigma}), \tag{5}$$

where the mean vector and (diagonal) covariance matrix are, respectively,

$$\boldsymbol{\mu}^T = (\bar{E}_{\rm sym}, \bar{L}_{\rm sym}, \bar{K}_{\rm sat}, \bar{K}_{\rm sym}, \bar{Q}_{\rm sat}, \bar{Q}_{\rm sym}, \bar{Z}_{\rm sat}, \bar{Z}_{\rm sym})$$

and

$$\boldsymbol{\Sigma} = \mathrm{diag}(\Sigma_{E_{\rm sym}}, \Sigma_{L_{\rm sym}}, \Sigma_{K_{\rm sat}}, \Sigma_{K_{\rm sym}}, \Sigma_{Q_{\rm sat}}, \Sigma_{Q_{\rm sym}}, \Sigma_{Z_{\rm sat}}, \Sigma_{Z_{\rm sym}}). \tag{6}$$

While the lower-order coefficients are quite well constrained experimentally [37–42], the higher-order $Q_{\rm sat}$, $Z_{\rm sat}$ $K_{\rm sym}$, $Q_{\rm sym}$, and $Z_{\rm sym}$ are poorly known [34,43–48]. In the present work, we fix $E_{\rm sat} = -15.8$ MeV and $n_0 = 0.155$ fm^{-3} as these quantities are rather well constrained. Table I shows the parameter means and standard deviations, $\sigma_a = \sqrt{\Sigma_a}$, we use [34].

Each valid EOS sampled describes $npe\mu$ matter in β equilibrium and satisfy the following conditions: (i) the pressure is an increasing function of density (thermodynamic stability); (ii) the speed of sound is smaller than the speed of light (causality); (iii) the EOS supports a maximum mass at least as high as 1.97 $M_\odot$ [1–4]. This EOS sampling approach introduces no *a priori* correlations between the parameters (zero covariances), and the correlations present in the final set of valid EOSs are solely induced from the above conditions. We use the nuclear SLy4 EOS [49] for the low density region of $n < 0.5n_0$, and a power-law interpolation between $0.5n_0 < n < n_0$ is performed to ensure a matching at n_0 with the sampled EOS (different matching procedures were analyzed in [50]).

Employing the EOS Taylor expansion around saturation for symmetric nuclear matter as the EOS parametrization itself is widely used [33–35,47,51–57]. There are no convergence issues when it is considered as an EOS parametrization, and this is a reliable approximation for realistic EOS around the saturation density for symmetric nuclear matter [33]. In [33] the authors have also shown that they could fit any EOS to a quite good accuracy using the EOS fourth-order Taylor expansion. However, the higher-order parameters must be seen as effective terms, which may substantially deviate from the actual nuclear matter expansion coefficients. Nevertheless, the present EOS parametrization allows one to directly constrain the EOS from the properties of symmetric nuclear matter and the symmetry energy near saturation density, while different EOS parametrizations impose such properties in a indirect way [47]. A recent work [58] has pointed out that the use of such Taylor expansion parametrization may be an inadequate approach. The authors have compared the results from two parametrization procedures: (i) a third-order Taylor expansion and (ii) a hybrid formulation where a second-order Taylor expansion describes matter below $2n_0$ and three polytropes are used to describe matter above that density. While we agree that the present EOS parametrization has its limitations, it should not be compared with a hybrid procedure where polytropes are randomly added to the low density Taylor expansion, as it breaks the correlations between the information around the saturation density, from the Taylor expansion, with the high density region defined by the polytropes. In this approach, the correlations among the Taylor coefficients and the polytropes indices are close to zero (which is visible in the posterior probabilities in [58]), and both low and high density regions are disconnected. Since we are only interested in constraining the thermodynamic properties of the EOS and not the nuclear matter properties, and we consider a one-branch EOS, the Taylor expansion is as reliable as other parametrizations, describing smooth equations of state.

For each EOS, we compute the dimensionless tidal deformability $\Lambda = \frac{2}{3} k_2 C^{-5}$, where k_2 is the quadrupole tidal Love number and $C = GM/(c^2 R)$ is the star's compactness [59]. We also determine the effective tidal deformability of binary systems:

$$\tilde{\Lambda} = \frac{16}{13} \frac{(12q+1)\Lambda_1 + (12+q)q^4\Lambda_2}{(1+q)^5}, \tag{7}$$

where $q = M_2/M_1 < 1$ is the binary mass ratio and $\Lambda_1(M_1)$ and $\Lambda_2(M_2)$ represent the tidal deformability (mass) of the primary and the secondary NS in the binary, respectively. $\tilde{\Lambda}$ is the leading tidal parameter in gravitational-wave signal from a NS merger. The constraint $\tilde{\Lambda} = 300^{+500}_{-190}$ (symmetric 90% credible interval) was estimated from the GW170817 with a mass ratio bounded as $0.73 \leq q \leq 1$ [12]. The binary chirp mass $M_{\rm chirp} = M_1 q^{3/5}/(1+q)^{1/5}$ was measured as $M_{\rm chirp} = 1.186^{+0.001}_{-0.001}\ M_\odot$ for the GW170817 event [12]. In the present work, we fix the $M_{\rm chirp}$ to 1.186 $M_\odot$.

III. RESULTS

By applying the statistical procedure described in the last section, we have generated a dataset containing 150000 EOSs that describe neutron star matter in β equilibrium.

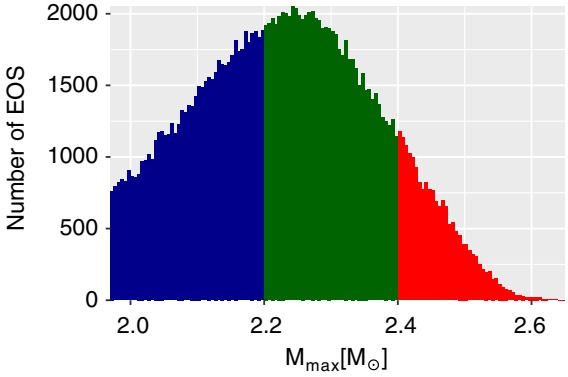

FIG. 1. Number of EOSs as a function of $M_{\rm max}$. The colors identify the subsets: $1.97 < M_{\rm max}/M_\odot \leq 2.20$ (blue), $2.20 < M_{\rm max}/M_\odot \leq 2.40$ (green), and $2.40 < M_{\rm max}/M_\odot \leq 2.66$ (red).

A. Subsets defined by $M_{\rm max}$

We are interested in studying the effect of the maximum NS mass $M_{\rm max}$ on the NS EOS properties. Therefore, we split our dataset into three subsets depending on $M_{\rm max}$ reached by each EOS: $1.97 < M_{\rm max}/M_\odot \leq 2.20$ (set 1), $2.20 < M_{\rm max}/M_\odot \leq 2.40$ (set 2), and $2.40 < M_{\rm max}/M_\odot \leq 2.66$ (set 3). The highest value reached in our dataset is $M_{\rm max} = 2.66\ M_\odot$. The histogram of the number of EOSs as a function of $M_{\rm max}$ is shown in Fig. 1, displaying a unimodal distribution with a peak around $2.25 M_\odot$, being the most likely outcome for $M_{\rm max}$ within the present EOS parametrization approach and sampling procedure. Only 3162 EOSs were able to sustain a NS with $M_{\rm max} > 2.5\ M_\odot$, 2.11% of our dataset.

Let us recall that different experiments have recently concentrated on getting more information on the nuclear symmetry energy at saturation. In [60], the authors have constrained the symmetry energy and its slope at saturation to, respectively, $32.5 < E_{\rm sym} < 38.1$ MeV and $42 < L_{\rm sym} < 110$ MeV using spectra of charged pions produced in intermediate-energy collisions. These values are in accordance with the ones obtained in [61] from charge exchange and elastic scattering reactions, respectively, $33.5 < E_{\rm sym} < 36.4$ MeV and $70 < L_{\rm sym} < 101$ MeV, but smaller than the ones determined from the measurement of the neutron radius of ^{208}Pb by the PREX-2 Collaboration [62,63], which have obtained for the slope of the symmetry energy $L_{\rm sym} = 106 \pm 37$ MeV. These estimates are somehow larger than the ones proposed in [40], which take into account experimental, theoretical and observational constraints, e.g., $29.0 < E_{\rm sym} < 32.7$ MeV and $44 < L_{\rm sym} < 66$ MeV ([40] and updated in [64]). The symmetry energy properties of our EOS (see Table II) essentially reproduce at one standard deviation the constraints of [64], which are strongly influenced by chiral effective field theory results for neutron matter [65]. However, the three sets also include EOSs that fall within the recent experimental intervals within 2–3 standard deviations. Moreover, the extremes are well out of these ranges.

TABLE II. The mean [MeV] and standard deviation [MeV] (std) of the EOS parameters for each set. In the following figures the different sets are represented by the colors blue (set 1), green (set 2) and red (set 3).

	Set 1		Set 2		Set 3	
$M_{\rm max}/M_\odot$	]1.97, 2.20]		]2.20, 2.40]		]2.40, 2.66]	
# EOSs	61660		69789		18551	
	Mean	Std	Mean	Std	Mean	Std
$K_{\rm sat}$	229.28	19.83	233.17	19.63	238.74	19.75
$Q_{\rm sat}$	−93.44	65.23	18.11	71.09	148.11	77.45
$Z_{\rm sat}$	−3.47	67.31	−109.11	81.75	−237.37	96.68
$E_{\rm sym}$	32.01	1.98	32.01	2.00	31.90	2.01
$L_{\rm sym}$	61.21	14.85	60.97	14.89	58.19	14.89
$K_{\rm sym}$	−64.06	90.62	−72.54	89.88	−107.78	78.87
$Q_{\rm sym}$	300.44	328.93	227.27	320.31	112.70	277.83
$Z_{\rm sym}$	392.77	684.98	292.95	598.48	433.28	509.64

Table II shows the mean and standard deviations of each set. We see that, except for $Z_{\rm sym}$, isovector properties decrease from set 1 to set 3. Larger $M_{\rm max}$ values require smaller isovector properties, while the isoscalar properties show the opposite behavior; e.g., $K_{\rm sat}$ increases slightly and there is a considerable increase of $Q_{\rm sat}$, but $Z_{\rm sat}$ shows a different behavior. Two comments are in order: (i) both $E_{\rm sym}$ and $L_{\rm sym}$ are very similar in the three sets, indicating that the maximum mass star is not sensitive to the symmetry energy close to saturation density; (ii) since $Z_{\rm sat}$ is the last term of the expansion considered, it has an effective character taking into account all the missed higher-order terms. As we mentioned in Sec. II, the high-order terms should be seen as effective ones, and their values might deviate from the true nuclear matter properties. A recent review [56] discussing the constraints set on the nuclear symmetry energy by NS observations since the detection of GW170817 proposes for the $L_{\rm sym}$ and $K_{\rm sym}$ values and uncertainties of the order of the ones presented in Table II.

1. Neutron star properties

In order to study NS properties, we integrate the Tolman-Oppenheimer-Volkoff equations [66,67], together with the differential equations that determine the tidal deformability [68]. Figure 2 shows the radius (left panel) and tidal deformability (right panel) as a function of the NS mass for each set. Statistics for some specific NS masses are given in Table III. As expected, larger $M_{\rm max}$ values correspond to larger NS radii and tidal deformabilities. The lower bound on R is more sensitive to $M_{\rm max}$ than the upper bound. However, we are unable to constrain the $M_{\rm max}$ value from the analysis of the

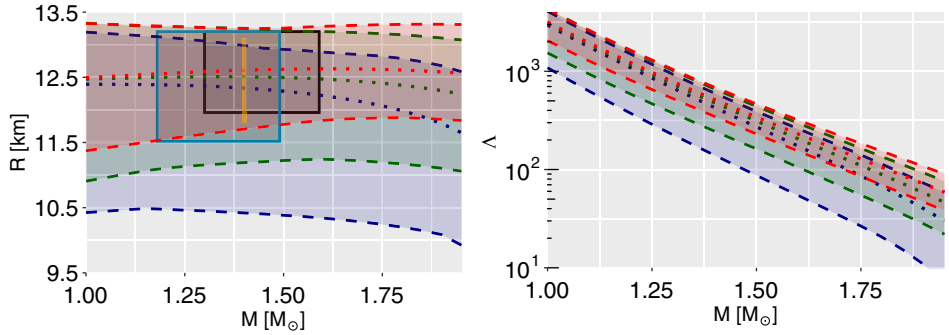

FIG. 2. The minimum and maximum (dashed lines) and mean (dotted lines) values for the radius (left panel) and tidal deformability (right panel) as a function of NS mass. The color indicates the set: set 1 (blue), set 2 (green), and set 3 (red). The regions enclosed by solid lines display (M, R) constraints obtained by two independent analysis using the NICER x-ray data from the millisecond pulsar PSR J0030 + 0451 [69,70], while the orange bar shows the recent constraint, $R_{1.4\,M_\odot} = 12.45 \pm 0.65$ km, extracted from a combination of NICER and XMM-Newton data [71].

millisecond pulsar PSR J0030 + 0451 (obtained from the NICER x-ray data) [69,70] since all sets describe the NICER data. Next, we will also conclude that we cannot constrain the $M_{\rm max}$ from the tidal deformability inferred from the GW170817 event [12].

Figure 3 shows the extreme values (maximum and minimum) for the tidal deformability from our entire dataset (left panel) and the effective tidal deformability of the binary ($M_{\rm chirp} = 1.186\ M_\odot$) as a function of the binary mass ratio $q = M_2/M_1$. Two main conclusions can be extracted: (i) the range of $\tilde{\Lambda}$ shifts to higher values as $M_{\rm max}$ increases, but all sets are compatible with $\tilde{\Lambda} = 300^{+500}_{-190}$ (symmetric 90% credible interval) from the GW170817 event [12]; (ii) furthermore, the NS tidal deformability range of our dataset is consistent with the 90% posterior credible level obtained in [32], when the analysis assumes that the EOS should describe 1.97 $M_\odot$ NS. Some statistics for the different sets are given in Table III.

Notice that in [72] the authors have obtained for the radius of a 1.4 $M_\odot$ star $12.33^{+0.76}_{-0.81}$ and $12.18^{+0.56}_{-0.79}$ km within two different models. The radii obtained within our sets (see Table III) are in accordance with these predictions. However, the prediction obtained for the radius of the PSR J0740 + 6620 in [71], $12.39^{+1.30}_{-0.98}$ km with mass $2.072^{+0.067}_{-0.066}\ M_\odot$ [7], seems to be more compatible with the two sets with larger maximum masses, although set 1 is not excluded.

We also give the prediction for the radius of a 1.6 $M_\odot$ star that has been constrained in [73] to be larger than $10.68^{+0.15}_{-0.04}$ km considering that there was no prompt collapse following GW170817 as suggested by the associated electromagnetic emission. All our three sets satisfy this constraint. As expected, the predicted central density of maximum mass stars decreases from the less massive set to the most massive. For the last set we have obtained a central density of $5.05 < n_{\rm max}/n_0 < 6.19$ compatible with the values proposed in [30] for cold nonspinning NSs.

2. EOS thermodynamics

Let us now analyze the thermodynamics properties of each EOS subset. The pressure and speed of sound are

TABLE III. Sample statistics for R_{M_i}, Λ_{M_i}, $\tilde{\Lambda}_{q=0.9}$, and the NS central density $n_{\rm max}/n_0$ and speed of sound squared $(v_s^{\rm cen})^2$ for the three sets considered.

	Set 1				Set 2				Set 3			
	$1.97 < M_{\rm max}/M_\odot \leq 2.20$				$2.20 < M_{\rm max}/M_\odot \leq 2.40$				$2.40 < M_{\rm max}/M_\odot \leq 2.66$			
	Mean	Std	Min	Max	Mean	Std	Min	Max	Mean	Std	Min	Max
$R_{1.4\,M_\odot}$ [km]	12.34	0.22	10.42	12.99	12.51	0.22	11.19	13.25	12.61	0.20	11.70	13.25
$R_{1.6\,M_\odot}$ [km]	12.22	0.24	10.34	12.89	12.47	0.21	11.24	13.20	12.63	0.20	11.84	13.28
$R_{2.08\,M_\odot}$ [km]	11.37	0.36	9.76	12.36	12.05	0.26	10.89	12.95	12.48	0.19	11.76	13.29
$\Lambda_{1.4\,M_\odot}$	427.36	50.37	139.55	598.21	477.83	50.23	245.1	660.47	514.68	47.29	346.4	688.17
$\Lambda_{1.6\,M_\odot}$	260.01	25.05	54.45	260.01	205.37	23.56	105.18	296.23	229.95	21.95	153.81	319.37
$\tilde{\Lambda}_{q=0.9}$	506.41	57.53	167.28	700.38	561.13	58.07	286.23	772.35	600.42	54.83	403.99	797.54
$n_{\rm max}/n_0$	7.09	0.42	5.72	8.65	6.35	0.27	5.51	7.32	5.76	0.16	5.05	6.19
$(v_s^{\rm cen})^2$ $[c^2]$	0.75	0.17	0.03	1	0.86	0.12	0.02	1	0.91	0.08	0.36	1

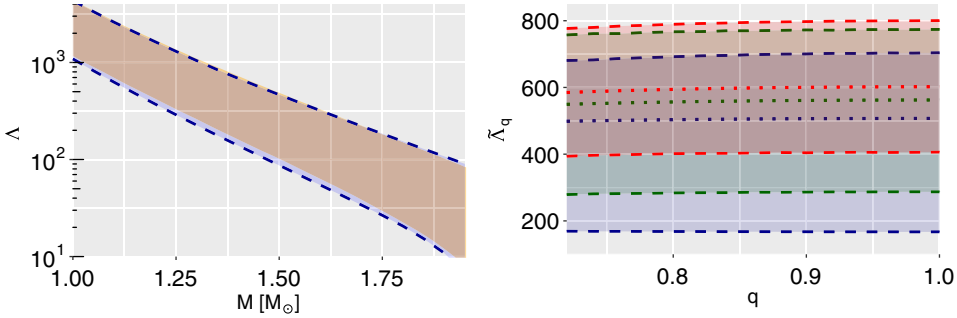

FIG. 3. Left panel: the tidal deformability minimum and maximum values (dashed lines) for the entire dataset, i.e., $1.97 < M_{\rm max}/M_\odot \leq 2.66$. The red region corresponds to the 90% posterior credible level obtained in [32], when it is imposed that the EOS should describe 1.97 $M_\odot$ NS. Right panel: the minimum and maximum (dashed lines) and mean (dotted lines) values for the effective tidal deformability of the binary, $\tilde{\Lambda}$, as a function of q with $M_{\rm chirp} = 1.186\ M_\odot$. The color indicates the set: set 1 (blue), set 2 (green), and set 3 (red).

shown in Fig. 4, where the shaded colored regions represent the 90% credible (equal-tailed) interval regions (sets 1, 2 and 3 are, respectively, blue, green and red). For the pressure (left panel), the results of each set begins to deviate from each other only at moderate densities, $n \approx 0.3$ fm^{-3}. Although the results are within the range of the LIGO/Virgo analysis (gray region), there is a considerable discrepancy for densities $n < 0.55$ fm^{-3}, although the extreme values cover a larger region. This is expected since the EOS parametrization we use is constrained at low densities by the low-order nuclear matter parameters, such as $L_{\rm sym}$ and $K_{\rm sat}$, while a polytropic approach such as the one used in the analysis of GW170917, being solely constrained by thermodynamic stability conditions, is able to reproduce extreme behaviors at any density region (even close to the saturation density).

The speed of sound (right panel of Fig. 4) also shows a similar dependence at low densities for all sets but a different prediction at higher densities. If we compare set 1 (blue), $1.97 < M_{\rm max}/M_\odot < 2.20$, with set 3 (red), $2.40 < M_{\rm max}/M_\odot < 2.66$, we see that the regions do not overlap for $n > 0.4$ fm^{-3}, showing that the high density dependence of v_s^2 is considerable bound to the $M_{\rm max}$ value. Moreover, the extremes show the possibility of a large softening of the EOS occurring, as would be present for a phase transition. These are the EOS that in the present approach cover the lower range of the $P(n)$ band determined by LIGO/Virgo Collaboration. On the other hand, the upper limit of the speed of sound is clearly defined by the causality constraint at high densities.

B. Constraining the EOS from $\tilde{\Lambda}$

The analysis of the GW170817 event by the LIGO/Virgo Collaboration has provided a constraint on the effective tidal deformability of the binary system, $\tilde{\Lambda} = 300^{+500}_{-190}$ (symmetric 90% credible interval) [12]. A possible way of learning how such a credible region constrains the properties of the nuclear matter consists in filtering out all EOSs that do not fulfill such interval and analyze the properties of the remaining EOSs. However, the set of EOSs used in the present study predicts $\tilde{\Lambda}$ values that range

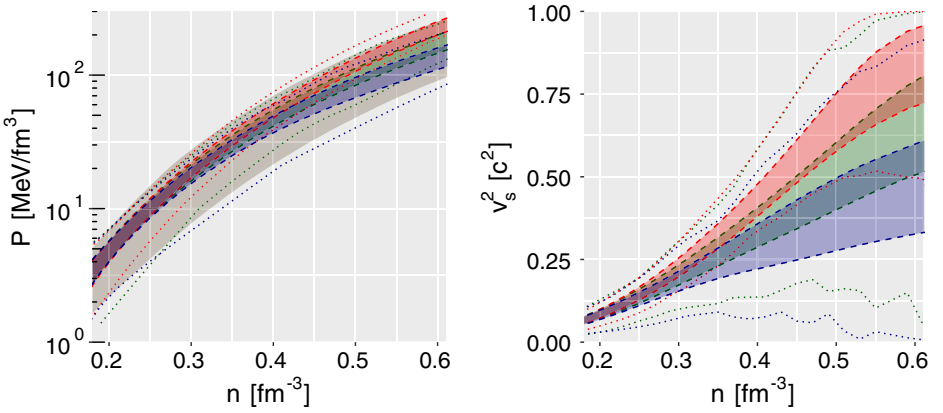

FIG. 4. The 90% credible levels (dashed lines) and maximum and minimum values (dotted lines) for the pressure (left) and speed of sound squared (right) as a function of baryonic density. The color identifies the set: set 1 (blue), set 2 (green), and set 3 (red). The gray region in $p(n)$ corresponds to the 90% posterior credible level from [13].

between 168 and 790 (sample minimum and maximum values), not reproducing either $110 < \tilde{\Lambda} < 168$ or $\tilde{\Lambda} > 790$; i.e., the smallest and largest values obtained from the GW170817 analysis are not represented in our set. Notice, however, that the kilonova and macronova AT2017gfo sets a lower bound on binary tidal deformability, which should satisfy, for the GW170817 event, $\tilde{\Lambda} > 200$ according to [74] or $\tilde{\Lambda} > 300$ according to [16,17], and, therefore, our lower bound is reasonable. Even though our set statistics presents a good agreement with $\tilde{\Lambda} = 300^{+500}_{-190}$ (see Table III), in the following we explore a probabilistic inference of the EOS using the entire information encoded in the probability distribution of $\tilde{\Lambda}$ for the GW170817 event [12] and a multivariate Gaussian distribution of the EOS based on the properties of our EOS sets. Note that the formalism developed in the present section considers the entire dataset, without any class subset related with the maximum mass $M_{\max}$.

1. Probability distributions for the pressure and speed of sound

We use a joint multivariate Gaussian distribution and its conditioning properties to constrain the EOS thermodynamics, namely $p(n)$ and $v_s^2(n)$. This allows us to consider the complete information encoded in the posterior PDF of $\tilde{\Lambda}$, $P_{LV}(\tilde{\Lambda})$ [12].

Let us consider a N-multivariate Gaussian probability distribution $P(z_1,z_2,\ldots,z_N)=\mathcal{N}(z_1,z_2,\ldots z_N;\boldsymbol{\mu},\boldsymbol{\Sigma})$, where $\boldsymbol{\mu} = (E[z_1], E[z_2], \ldots E[z_N])^T$ represents the mean vector and $\Sigma_{ij} = E[(z_i - \mu_i)(z_j - \mu_j)]$ are the covariance matrix entries (E represents the expected value operator). To simplify the notation, let us rewrite the above probability distribution as

$$\mathcal{N}(z_1, z_2, \ldots z_N;\boldsymbol{\mu},\boldsymbol{\Sigma}) = \mathcal{N}(\mathbf{X},\mathbf{Y};\boldsymbol{\mu},\boldsymbol{\Sigma}), \tag{8}$$

where $\mathbf{X} = (z_1, \ldots, z_q)^T$ and $\mathbf{Y} = (z_{q+1}, \ldots, z_N)^T$ are, respectively, two subsets with dimension q and $N-q$ of the original N random variables. This way, the mean vector and covariance matrix are partitioned into blocks:

$$\boldsymbol{\mu} = \begin{pmatrix} E[\mathbf{X}] \\ E[\mathbf{Y}] \end{pmatrix} \equiv \begin{pmatrix} \boldsymbol{\mu}_\mathbf{X} \\ \boldsymbol{\mu}_\mathbf{Y} \end{pmatrix} \quad \text{and} \quad \boldsymbol{\Sigma} = \begin{pmatrix} \boldsymbol{\Sigma}_{\mathbf{XX}} & \boldsymbol{\Sigma}_{\mathbf{XY}} \\ \boldsymbol{\Sigma}_{\mathbf{YX}} & \boldsymbol{\Sigma}_{\mathbf{YY}} \end{pmatrix}, \tag{9}$$

respectively. For instance, the block $\boldsymbol{\Sigma}_{\mathbf{XY}}$ is a $q \times (N-q)$ matrix with the (1,1) entry being $E[(z_1 - \mu_1) \times (z_{q+1} - \mu_{q+1})]$.

A crucial operation for Gaussian distributions is the conditional probability. It allows us to determine the probability of a set of variables depending (conditioning) on the other set variables, yielding a modified—but still—Gaussian probability distribution. Conditioning the PDF $P(\mathbf{X},\mathbf{Y}) = \mathcal{N}(\mathbf{X},\mathbf{Y};\boldsymbol{\mu},\boldsymbol{\Sigma})$ upon the set variables $\mathbf{Y}$ gives

$$P(\mathbf{X}|\mathbf{Y}) = \mathcal{N}(\mathbf{X}|\mathbf{Y};\bar{\boldsymbol{\mu}},\bar{\boldsymbol{\Sigma}}), \tag{10}$$

where

$$\bar{\boldsymbol{\mu}} = \boldsymbol{\mu}_\mathbf{X} + \boldsymbol{\Sigma}_{\mathbf{XY}}\boldsymbol{\Sigma}_{\mathbf{YY}}^{-1}(\mathbf{Y} - \boldsymbol{\mu}_\mathbf{Y}), \tag{11}$$

$$\bar{\boldsymbol{\Sigma}} = \boldsymbol{\Sigma}_{\mathbf{XX}} - \boldsymbol{\Sigma}_{\mathbf{XY}}\boldsymbol{\Sigma}_{\mathbf{YY}}^{-1}\boldsymbol{\Sigma}_{\mathbf{YX}}. \tag{12}$$

The dimensions of the mean vector $\bar{\boldsymbol{\mu}}$ and of the covariance matrix $\bar{\boldsymbol{\Sigma}}$ are $q \times 1$ and $q \times q$, respectively.

Our goal is to infer the thermodynamic properties of the EOS from the knowledge of $\tilde{\Lambda}$, extracted from the GW170817 event. Given the current uncertainty on the $M_{\max}$, we want to analyze how the EOS inference depends on the $M_{\max}$ value. In the following, we consider the EOS pressure $p(n)$ and speed of sound $v_s^2(n)$. For each density n, we model the probability distributions $P(p(n), M_{\max}, \tilde{\Lambda})$ and $P(v_s^2(n), M_{\max}, \tilde{\Lambda})$ as multivariate Gaussian distributions [Eq. (8)], where both the mean vector and covariance matrix have a density dependence. Then, we condition upon $\tilde{\Lambda}$, i.e., $P(p(n), M_{\max}|\tilde{\Lambda})$ and $P(v_s^2(n), M_{\max}|\tilde{\Lambda})$ by applying Eq. (10), where $\mathbf{X}$ corresponds to $(p(n), M_{\max})^T$ and $(v_s^2(n), M_{\max})^T$, respectively, whereas $\mathbf{Y} = (\tilde{\Lambda})$. Next, we determine the joint probability distributions $P(p(n), M_{\max})$ and $P(v_s^2(n), M_{\max})$, by marginalizing over $\tilde{\Lambda}$, weighting by the prior PDF $P_{LV}(\tilde{\Lambda})$ [12]:

$$P(p(n), M_{\max}) = \int P(p(n), M_{\max}|\tilde{\Lambda}) P_{LV}(\tilde{\Lambda}) d\tilde{\Lambda}, \tag{13}$$

$$P(v_s^2(n), M_{\max}) = \int P(v_s^2(n), M_{\max}|\tilde{\Lambda}) P_{LV}(\tilde{\Lambda}) d\tilde{\Lambda}. \tag{14}$$

The probability distribution $P(p(n), M_{\max})$ is no longer Gaussian, due to the non-Gaussian characteristic of the prior $P_{LV}(\tilde{\Lambda})$. To obtain the probability distribution for the pressure, given a specific value of $M_{\max}$, say $M_{\max} = a$, we calculate $P(p(n)|M_{\max} = a) = P(p(n), M_{\max} = a)/P(M_{\max} = a)$. Finally, we characterize this PDF using symmetric 90% credible intervals. The same procedure is applied for the speed of sound. Equations (13) and (14) can be interpreted as compound PDFs. Note that any PDF can be thought as a marginal of some (higher dimension) joint PDF, e.g., $P(p(n), M_{\max}) = \int P(p(n), M_{\max}, \tilde{\Lambda}) d\tilde{\Lambda}$, and, furthermore, any joint PDF can be written as a conditional PDF, e.g., $P(p(n), M_{\max}, \tilde{\Lambda}) = P(p(n), M_{\max}|\tilde{\Lambda}) P(\tilde{\Lambda})$. That is, Eqs. (13) and (14) become trivial identities if we change $P_{LV}(\tilde{\Lambda})$ by the (dataset) marginal distribution $P(\tilde{\Lambda})$. Compound PDFs arise when one uses an "external" PDF for some of the probabilistic model variables; i.e., we are integrating

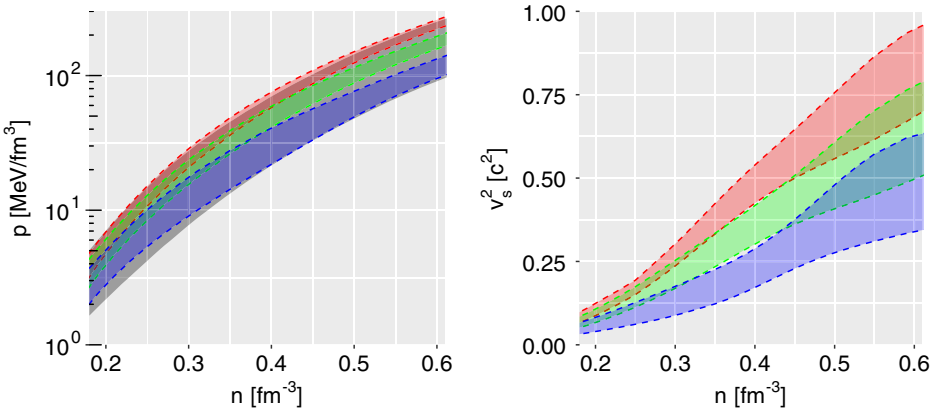

FIG. 5. Inference results for the pressure (left) and speed of sound squared (right) as a function of baryonic density. The color regions show the 90% credible intervals for the PDFs $P(p(n)|M_{\rm max})$ (left) and $P(v_s^2(n)|M_{\rm max})$ (right) for three values of $M_{\rm max}/M_\odot$: 2.0 (blue), 2.3 (green), and 2.6 (red). The gray region in the $p(n)$ plot corresponds to the 90% posterior credible level from [13].

out $\tilde{\Lambda}$ from our probabilistic models $P(p(n), M_{\rm max}|\tilde{\Lambda})$ and $P(v_s^2(n), M_{\rm max}|\tilde{\Lambda})$ by weighting each value of $\tilde{\Lambda}$ by a specific (prior) PDF, which has a different structure than the dataset $P(\tilde{\Lambda})$.

Figure 5 shows the results for $P(p(n)|M_{\rm max})$ (left) and $P(v_s^2(n)|M_{\rm max})$ (right), for three values of $M_{\rm max}/M_\odot$: 2.0 (red), 2.3 (green), and 2.6 (blue). The gray band on the $P(n)$ plot indicates the prediction region determined by the LIGO/Virgo analysis [13]. It is interesting to conclude that (i) the bands do not overlap (i.e., knowing the maximum star mass it is possible to extract quite constrained information on the high density EOS); (ii) the three bands obtained with different maximum masses lie almost inside the 90% credible interval predicted from the GW170817 by LIGO/Virgo, obtained imposing that a maximum star mass equal to 1.97 $M_\odot$, the main difference lying on the upper boundary corresponding to the more massive stars; and (iii) the probabilistic approach which allows one to take into account the whole GW170817 PDF has given more freedom to the low density EOS, giving rise to distinct bands also at low densities contrary to the previous conclusions. The $p(n)$ band obtained by the LIGO/Virgo Collaboration was obtained from a set of EOSs not constrained by nuclear matter properties and, therefore, may cover a region that would be excluded by nuclear properties.

Using the probabilistic model, it was possible to determine the expected pressure band for a maximum star mass within a well-defined mass range. For mass intervals that take as the lower limit observed two solar mass stars the lower limit of the LIGO/Virgo Collaboration pressure band is not populated at 90% credible probability. For the speed of sound, a monotonic increasing function of the density, values quite far from the conformal limit were obtained. The maximum mass clearly constrains the speed of sound, with values close to one being obtained only if a maximum mass of 2.66 $M_\odot$ is imposed. The main effect of the probabilistic approach that takes into account the full PDF obtained by the LIGO/Virgo Collaboration for the tidal deformability with respect to the study done in the

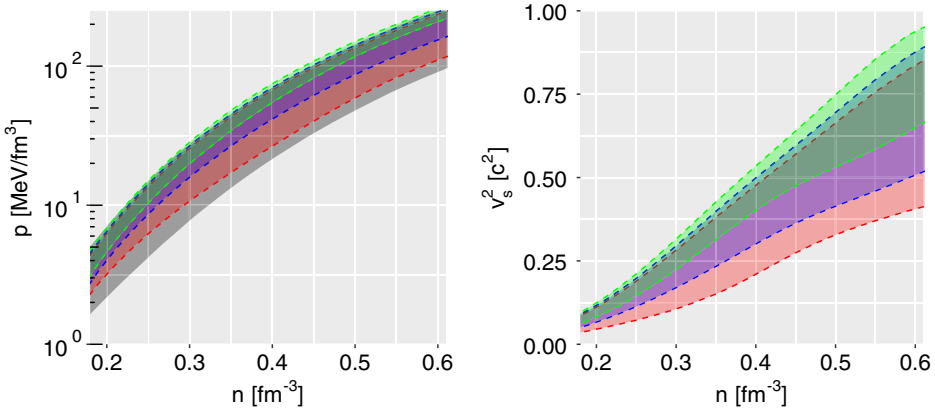

FIG. 6. Inference results for the pressure (left) and speed of sound squared (right) as a function of baryonic density. The red, blue, and green regions indicate the 90% credible intervals for $M_{\rm max}/M_\odot \in [2.0, 2.66]$, $\in [2.2, 2.66]$, and $\in [2.5, 2.66]$, respectively. The gray region corresponds to the 90% posterior credible level from [13].

previous section is to enlarge the speed of sound range at low densities, allowing for quite low values of the speed of sound and, therefore, giving rise to a harder EOS at intermediate densities.

Instead of a fixed value for $M_{\rm max}$, we can consider an interval by determining $P(p(n)) = \int_a^b P(p(n), M_{\rm max}) dM_{\rm max}$. The results are in Fig. 6. Two main conclusions can be drawn: (i) the detection of NS with a mass above two solar masses that decreases the NS maximum mass uncertainty interval from below will help constraining the high density EOS (future observation from Square Kilometer Array will certainly bring information on this lower limit); (ii) taking as hypothesis a one-branch mass-radius NS curve and imposing maximum masses above two solar masses does not allow one to cover the whole pressure-density range defined by the LIGO/Virgo Collaboration for the GW170817 binary NS merger.

IV. CONCLUSIONS

In the present study we have studied the possibility of constraining the EOS from the knowledge of the NS maximum mass $M_{\rm max}$, starting from the hypothesis of an EOS with no first-order phase transition, and, as a second objective, we have shown how to use the entire information obtained from the GW170817 event for the probability distribution of $\tilde{\Lambda}$ to make a probabilistic inference of the EOS. We have generated a set of 150000 EOSs that are constrained at low densities, saturation density and below, by nuclear properties. Otherwise, these EOSs were required to be thermodynamically consistent, casual and to describe NS with maximum masses above 1.97 $M_\odot$. In a first step the EOS set was divided into three subsets corresponding to three intervals for the maximum mass, e.g., [1.97, 2.2] $M_\odot$, [2.2,2.4] $M_\odot$ and above 2.4 $M_\odot$ and the pressure of catalyzed beta-equilibrium neutral matter was obtained as a function of the baryonic density. It was shown that, while at low densities the pressure band obtained for each set coincides below 2 times saturation density, above these densities the differences are large and the pressure and speed of sound of the extreme sets (the lowest and largest mass sets) do not overlap, showing that the knowledge of the NS maximum mass may give some information on the high density EOS. These sets, however, do not cover the whole EOS band predicted by the GW170817 event [32]. The set we are using is more restrictive at low densities, since the EOS set used in the GW170817 analysis does not take into account nuclear properties. Recently some tension between observational data and the nuclear physics inputs and on the deformability probability distribution depending on the inclusion or not of multimessenger information was discussed in [55]. In particular, this analysis discusses the implications on the nuclear matter EOS properties.

We have next used a probabilistic approach based on our complete EOS dataset in order to use all the information the GW170817 gives us. This has allowed us to explore a region of the EOS phase space that was not accessible if nuclear matter properties close to saturation density are imposed. It is shown that it is possible to extract constrained information on the high density EOS from the knowledge of the maximum mass. In particular, it was shown that the 90% credible intervals of the pressure as a function of the baryonic density obtained considering a maximum mass of 2 $M_\odot$, 2.3 $M_\odot$ and 2.6 $M_\odot$ do not overlap for densities above 0.45 fm^{-3}. Moreover, neither the pressure nor the speed of sound 90% credible intervals considering the two maximum masses 2 $M_\odot$ and 2.6 $M_\odot$ overlap for any density above saturation density. This seems to indicate that determining the NS maximum mass will give us strong constraints on the EOS at high densities. In particular, the detection of more massive NS will narrow the uncertainty on the high density EOS. It was also shown that the speed of sound increases monotonically well above the conformal limit and that a maximum mass of the order of 2.6 $M_\odot$ may push the upper limit of the speed of sound to $\sim$1 at $4n_0$. However, there is also a finite probability of obtaining an EOS that satisfies $v_s^2 \lesssim 1/3$ if the maximum mass is close to 2 $M_\odot$.

ACKNOWLEDGMENTS

This work was partially supported by national funds from FCT (Fundação para a Ciência e a Tecnologia, I.P, Portugal) under Projects No. UID/FIS/04564/2019, No. UID/04564/2020, and No. POCI-01-0145-FEDER-029912 with financial support from Science, Technology and Innovation, in its FEDER component, and by the FCT/MCTES budget through national funds (OE).

[1] Z. Arzoumanian *et al.* (NANOGrav Collaboration), Astrophys. J. Suppl. **235**, 37 (2018).
[2] E. Fonseca *et al.*, Astrophys. J. **832**, 167 (2016).
[3] P. Demorest, T. Pennucci, S. Ransom, M. Roberts, and J. Hessels, Nature (London) **467**, 1081 (2010).
[4] J. Antoniadis *et al.*, Science **340**, 1233232 (2013).
[5] H. T. Cromartie *et al.*, Nat. Astron. **4**, 72 (2020).
[6] E. Fonseca *et al.*, Astrophys. J. Lett. **915**, L12 (2021).
[7] T. E. Riley *et al.*, arXiv:2105.06980.
[8] Z. Arzoumanian *et al.*, The neutron star interior composition explorer (NICER): mission definition, in *Proceedings of the SPIE*, Society of Photo-Optical Instrumentation Engineers

(SPIE) Conference Series Vol. 9144 (SPIE, Bellingham, WA, 2014), p. 914420.
[9] T. E. Riley, A. L. Watts, S. Bogdanov, P. S. Ray, R. M. Ludlam, S. Guillot, Z. Arzoumanian, C. L. Baker, A. V. Bilous, D. Chakrabarty, K. C. Gendreau, A. K. Harding, W. C. G. Ho, J. M. Lattimer, S. M. Morsink, and T. E. Strohmayer, Astrophys. J. **887**, L21 (2019).
[10] M. C. Miller *et al.*, Astrophys. J. **887**, L24 (2019).
[11] B. P. Abbott *et al.* (LIGO Scientific, Virgo Collaborations), Phys. Rev. Lett. **119**, 161101 (2017).
[12] B. P. Abbott *et al.* (LIGO Scientific, Virgo Collaborations), Phys. Rev. X **9**, 011001 (2019).
[13] B. P. Abbott *et al.* (Virgo, LIGO Scientific Collaborations), Phys. Rev. Lett. **121**, 161101 (2018).
[14] B. P. Abbott *et al.* (LIGO Scientific, Virgo, Fermi-GBM, INTEGRAL Collaborations), Astrophys. J. **848**, L13 (2017).
[15] B. P. Abbott *et al.* (LIGO Scientific, Virgo, Fermi GBM, INTEGRAL, IceCube, AstroSat Cadmium Zinc Telluride Imager Team, IPN, Insight-Hxmt, ANTARES, Swift, AGILE Team, 1M2H Team, Dark Energy Camera GW-EM, DES, DLT40, GRAWITA, Fermi-LAT, ATCA, ASKAP, Las Cumbres Observatory Group, OzGrav, DWF (Deeper Wider Faster Program), AST3, CAASTRO, VINROUGE, MASTER, J-GEM, GROWTH, JAGWAR, CaltechNRAO, TTU-NRAO, NuSTAR, Pan-STARRS, MAXI Team, TZAC Consortium, KU, Nordic Optical Telescope, ePESSTO, GROND, Texas Tech University, SALT Group, TOROS, BOOTES, MWA, CALET, IKI-GW Follow-up, H.E.S.S., LOFAR, LWA, HAWC, Pierre Auger, ALMA, Euro VLBI Team, Pi of Sky, Chandra Team at McGill University, DFN, ATLAS Telescopes, High Time Resolution Universe Survey, RIMAS, RATIR, SKA South Africa/MeerKAT Collaborations), Astrophys. J. **848**, L12 (2017).
[16] D. Radice, A. Perego, F. Zappa, and S. Bernuzzi, Astrophys. J. Lett. **852**, L29 (2018).
[17] D. Radice and L. Dai, Eur. Phys. J. A **55**, 50 (2019).
[18] A. Bauswein, N.-U. Friedrich Bastian, D. Blaschke, K. Chatziioannou, J. A. Clark, T. Fischer, H.-T. Janka, O. Just, M. Oertel, and N. Stergioulas, AIP Conf. Proc. **2127**, 020013 (2019).
[19] M. W. Coughlin *et al.*, Mon. Not. R. Astron. Soc. **480**, 3871 (2018).
[20] Y.-Z. Wang, D.-S. Shao, J.-L. Jiang, S.-P. Tang, X.-X. Ren, F.-W. Zhang, Z.-P. Jin, Y.-Z. Fan, and D.-M. Wei, Astrophys. J. **877**, 2 (2019).
[21] R. Abbott *et al.* (LIGO Scientific, Virgo Collaborations), Astrophys. J. Lett. **896**, L44 (2020).
[22] M. Shibata, S. Fujibayashi, K. Hotokezaka, K. Kiuchi, K. Kyutoku, Y. Sekiguchi, and M. Tanaka, Phys. Rev. D **96**, 123012 (2017).
[23] B. Margalit and B. D. Metzger, Astrophys. J. **850**, L19 (2017).
[24] J. Alsing, H. O. Silva, and E. Berti, Mon. Not. R. Astron. Soc. **478**, 1377 (2018).
[25] L. Rezzolla, E. R. Most, and L. R. Weih, Astrophys. J. Lett. **852**, L25 (2018).
[26] M. Shibata, E. Zhou, K. Kiuchi, and S. Fujibayashi, Phys. Rev. D **100**, 023015 (2019).
[27] A. Li, Z. Miao, S. Han, and B. Zhang, Astrophys. J. **913**, 27 (2021).
[28] M. Ruiz, S. L. Shapiro, and A. Tsokaros, Phys. Rev. D **97**, 021501 (2018).
[29] E. Annala, T. Gorda, E. Katerini, A. Kurkela, J. Nättilä, V. Paschalidis, and A. Vuorinen, arXiv:2105.05132.
[30] I. Legred, K. Chatziioannou, R. Essick, S. Han, and P. Landry, arXiv:2106.05313 [Phys. Rev. D (to be published)].
[31] P. T. H. Pang, I. Tews, M. W. Coughlin, M. Bulla, C. Van Den Broeck, and T. Dietrich, arXiv:2105.08688.
[32] B. P. Abbott *et al.* (LIGO Scientific, Virgo Collaborations), Phys. Rev. Lett. **121**, 161101 (2018).
[33] J. Margueron, R. Hoffmann Casali, and F. Gulminelli, Phys. Rev. C **97**, 025805 (2018).
[34] J. Margueron, R. Hoffmann Casali, and F. Gulminelli, Phys. Rev. C **97**, 025806 (2018).
[35] J. Margueron and F. Gulminelli, Phys. Rev. C **99**, 025806 (2019).
[36] M. Ferreira, M. Fortin, T. Malik, B. Agrawal, and C. Providência, Phys. Rev. D **101**, 043021 (2020).
[37] D. H. Youngblood, H. L. Clark, and Y. W. Lui, Phys. Rev. Lett. **82**, 691 (1999).
[38] J. Margueron and E. Khan, Phys. Rev. C **86**, 065801 (2012).
[39] B.-A. Li and X. Han, Phys. Lett. B **727**, 276 (2013).
[40] J. M. Lattimer and Y. Lim, Astrophys. J. **771**, 51 (2013).
[41] J. R. Stone, N. J. Stone, and S. A. Moszkowski, Phys. Rev. C **89**, 044316 (2014).
[42] M. Oertel, M. Hempel, T. Klähn, and S. Typel, Rev. Mod. Phys. **89**, 015007 (2017).
[43] M. Farine, J. M. Pearson, and F. Tondeur, Nucl. Phys. **A615**, 135 (1997).
[44] J. N. De, S. K. Samaddar, and B. K. Agrawal, Phys. Rev. C **92**, 014304 (2015).
[45] C. Mondal, B. K. Agrawal, J. N. De, and S. K. Samaddar, Phys. Rev. C **93**, 044328 (2016).
[46] T. Malik, N. Alam, M. Fortin, C. Providência, B. K. Agrawal, T. K. Jha, B. Kumar, and S. K. Patra, Phys. Rev. C **98**, 035804 (2018).
[47] N.-B. Zhang, B.-A. Li, and J. Xu, Astrophys. J. **859**, 90 (2018).
[48] B.-A. Li, P. G. Krastev, D.-H. Wen, W.-J. Xie, and N.-B. Zhang, AIP Conf. Proc. **2127**, 020018 (2019).
[49] F. Douchin and P. Haensel, Astron. Astrophys. **380**, 151 (2001).
[50] M. Ferreira and C. Providência, Universe **6**, 220 (2020).
[51] Z. Carson, A. W. Steiner, and K. Yagi, Phys. Rev. D **99**, 043010 (2019).
[52] I. Tews, J. Margueron, and S. Reddy, Phys. Rev. C **98**, 045804 (2018).
[53] W.-J. Xie and B.-A. Li, Astrophys. J. **883**, 174 (2019).
[54] M. Ferreira, R. Câmara Pereira, and C. Providência, Phys. Rev. D **102**, 083030 (2020).
[55] H. Güven, K. Bozkurt, E. Khan, and J. Margueron, Phys. Rev. C **102**, 015805 (2020).
[56] B.-A. Li, B.-J. Cai, W.-J. Xie, and N.-B. Zhang, Universe **7**, 182 (2021).
[57] N.-B. Zhang and B.-A. Li, arXiv:2105.11031.
[58] B. Biswas, P. Char, R. Nandi, and S. Bose, Phys. Rev. D **103**, 103015 (2021).

[59] T. Hinderer, Astrophys. J. **677**, 1216 (2008).
[60] J. Estee *et al.* (SRIT Collaboration), Phys. Rev. Lett. **126**, 162701 (2021).
[61] P. Danielewicz, P. Singh, and J. Lee, Nucl. Phys. **A958**, 147 (2017).
[62] D. Adhikari *et al.* (PREX Collaboration), Phys. Rev. Lett. **126**, 172502 (2021).
[63] B. T. Reed, F. J. Fattoyev, C. J. Horowitz, and J. Piekarewicz, Phys. Rev. Lett. **126**, 172503 (2021).
[64] J. M. Lattimer and A. W. Steiner, Eur. Phys. J. A **50**, 40 (2014).
[65] K. Hebeler, J. M. Lattimer, C. J. Pethick, and A. Schwenk, Astrophys. J. **773**, 11 (2013).
[66] R. C. Tolman, Phys. Rev. **55**, 364 (1939).
[67] J. R. Oppenheimer and G. M. Volkoff, Phys. Rev. **55**, 374 (1939).
[68] T. Hinderer, B. D. Lackey, R. N. Lang, and J. S. Read, Phys. Rev. D **81**, 123016 (2010).
[69] T. E. Riley, A. L. Watts, S. Bogdanov, P. S. Ray, R. M. Ludlam, S. Guillot, Z. Arzoumanian, C. L. Baker, A. V. Bilous, D. Chakrabarty, K. C. Gendreau, A. K. Harding, W. C. G. Ho, J. M. Lattimer, S. M. Morsink, and T. E. Strohmayer, Astrophys. J. **887**, L21 (2019).
[70] M. Miller *et al.*, Astrophys. J. Lett. **887**, L24 (2019).
[71] M. C. Miller *et al.*, arXiv:2105.06979.
[72] G. Raaijmakers, S. K. Greif, K. Hebeler, T. Hinderer, S. Nissanke, A. Schwenk, T. E. Riley, A. L. Watts, J. M. Lattimer, and W. C. G. Ho, arXiv:2105.06981.
[73] A. Bauswein, O. Just, H.-T. Janka, and N. Stergioulas, Astrophys. J. **850**, L34 (2017).
[74] K. Kiuchi, K. Kyutoku, M. Shibata, and K. Taniguchi, Astrophys. J. **876**, L31 (2019).